Research Square

Preprints are preliminary reports that have not undergone peer review.
They should not be considered conclusive, used to inform clinical practice,
or referenced by the media as validated information.

Multi-Physics Coupled Modeling and Predictive Control of the DLP Photocuring Printing Process

Pengbing Zhao

pbzhao@xidian.edu.cn

Xidian University

Mengyao Chen

Xidian University

Zheng Gao

Xidian University

Yize Chen

Xidian University

Jin Huang

Xidian University

Jianjun Wang

Xidian University

Jie Zhang

Xidian University

Hongxiao Gong

Xidian University

Research Article

Keywords: Additive manufacturing, Digital light processing, Multiphysics modeling, Model predictive control

Posted Date: September 10th, 2026

DOI: https://doi.org/10.21203/rs.3.rs-10409005/v1

License: This work is licensed under a Creative Commons Attribution 4.0 International License.
Read Full License

Additional Declarations: No competing interests reported.

Multi-Physics Coupled Modeling and Predictive Control of the DLP Photocuring Printing Process

Abstract

To address the loss of forming quality caused by the strong multiphysics coupling in digital light processing (DLP)-based vat photopolymerization additive manufacturing, this study proposes an integrated framework incorporating multiphysics modeling, key parameter identification, and advanced control strategies. First, a nonlinear state-space model describing the coupled evolution of optical, chemical, thermal, and mechanical fields was established based on the Beer–Lambert law, curing kinetics, and one-dimensional transient heat conduction theory. Subsequently, the kinetic parameters were identified through ultraviolet differential scanning calorimetry (UV-DSC) experiments. An indirect validation method based on DSC heat-flow signals was further proposed, where a capture factor was introduced to map the equivalent heat flow, thereby verifying the correctness of the coupled heat-generation and heat-transfer terms in the model. At the control level, a nonlinear model predictive control (NMPC) strategy integrated with a sliding mode observer (SMO) was developed, and a multilayer perceptron (MLP) neural network was introduced to assist prediction and improve real-time regulation performance. Fourier transform infrared spectroscopy (FTIR) experiments and variable light-intensity strategies demonstrated that the proposed control system significantly improved curing uniformity along the thickness direction. Comparison with COMSOL simulations showed that the proposed model achieved prediction errors of only approximately 1% for both degree of cure and temperature, while also effectively predicting the warpage trend of printed structures. The results provide important theoretical support for achieving shape and property control in photopolymerization additive manufacturing processes.

Keywords: Additive manufacturing, Digital light processing, Multiphysics modeling, Model predictive control

1. Introduction

Since its emergence in the 1980s, additive manufacturing (AM) has become a key enabling technology in advanced manufacturing fields such as biomedical engineering, aerospace, and precision manufacturing, owing to its capability for the direct fabrication of complex geometries[1, 2]. Among various AM approaches, digital light processing (DLP)-based photopolymerization has demonstrated significant potential for fabricating high-performance functional devices because of its superior printing resolution and excellent surface quality[3, 4]. In the DLP process, spatially controlled ultraviolet (UV) irradiation induces rapid chemical crosslinking of photosensitive resin, enabling the layer-by-layer fabrication of three-dimensional structures. However, the photopolymerization process is intrinsically a highly coupled multiphysics phenomenon involving radiation transport, polymerization kinetics, transient heat conduction, and dynamic stress evolution[5, 6]. The nonlinear interactions among these physical fields result in pronounced spatiotemporal nonuniformity in the curing process, which not only causes warpage deformation but also severely limits the consistency of mechanical properties in printed parts.

With the rapid development of Industry 4.0 and intelligent manufacturing, high-precision additive manufacturing has imposed increasing demands on process modeling and closed-loop control[7]. Current industrial practice still relies heavily on empirical open-loop parameter settings, which are insufficient to address uncertainties arising from material batch variations and environmental disturbances. Moreover, key state variables during photopolymerization, such as curing depth, internal temperature, and degree of conversion, exhibit strong transient characteristics and are difficult to measure directly in situ. Therefore, developing a closed-loop framework capable of characterizing multiphysics coupling mechanisms while enabling real-time state estimation and control has become a critical scientific challenge for achieving shape and property control in photopolymerization manufacturing.

1.1. Related Works

In the study of photopolymerization mechanisms, extensive efforts have been devoted to investigating the influence of process parameters on curing behavior. Emami [8] et al. established an optical field model based on Gaussian beam theory and quantified the influence of optical effects on the sidewall accuracy of micro/nanostructures. Par [9] et al. developed a coupled model relating resin viscosity, degree of conversion, and linear shrinkage through real-time radiance measurements. Regarding constitutive behavior, Valizadeh [10] et al. reduced process parameters into a unified "exposure intensity" variable and proposed a modified model for predicting viscoelastoplastic properties, whereas Xiang [11] et al. developed a physics-based viscohyperelastic model through tensile experiments under multiple light intensities. Furthermore, to overcome the thickness limitations of conventional photopolymerization, Petko [12] et al. and Kangmin [13] et al. pro-

posed optimization strategies based on dual-curing systems and dark-curing initiators, respectively, thereby providing theoretical support for the fabrication of large-scale and highly homogeneous structures.

In the field of process modeling and numerical simulation, constructing models capable of describing the dynamic evolution of multiphysics coupling is essential for predictive manufacturing. Wu [14] et al. combined FTIR and DMA experiments to establish a coupled kinetic and nonlinear viscoelastic model with the degree of conversion as an internal variable, successfully predicting residual stress and deformation in thick samples. Lang [15] et al. systematically reviewed photopolymerization kinetic modeling approaches from both phenomenological and mechanistic perspectives, providing guidelines for model selection. For complex system evolution, Rehbein [16] et al. developed a generalized Maxwell model dependent on temperature and degree of cure to evaluate interlayer separation forces, while Jiang [17] et al. proposed a micro–meso–macro multiscale model and addressed shadow attenuation in fiber-reinforced composites through a photothermal coupling strategy. Nevertheless, despite the high accuracy of these high-fidelity models, their substantial computational cost limits their applicability in real-time control scenarios.

In terms of process control and intelligent monitoring, research focus has gradually shifted from open-loop parameter optimization toward real-time closed-loop regulation. Thomas [18] et al. achieved feedback regulation of ceramic slurry curing rates using in situ infrared monitoring combined with a proportional–integral (PI) controller. Singh [19] et al. employed piezoelectric sensing to monitor storage modulus and introduced fuzzy logic control to suppress overcuring overshoot. With the rise of data-driven methods, Zhao [20] et al. combined long short-term memory (LSTM) networks with DLP printing systems to achieve millisecond-level temperature prediction and control strategy planning, while Zhang [21] et al. utilized machine learning for nonintrusive full-field monitoring of the curing degree. Although these approaches improved manufacturing repeatability, Sachdeva [22] et al. pointed out that existing strategies still face challenges in robustness and real-time predictive capability when dealing with DLP systems characterized by strongly coupled multistate dynamics and partially unmeasurable key states, such as internal temperature and curing gradients.

In summary, substantial progress has been achieved in revealing curing mechanisms and constructing complex multiphysics models. However, due to practical limitations such as unmeasurable system states and physical constraints, developing a simplified physics-based model with accurate parameter identification, and further integrating it into a closed-loop control framework with both physical interpretability and real-time capability, remains a critical challenge for intelligent photopolymerization manufacturing and high-precision consistent fabrication.

1.2. Outline

This study aims to develop an integrated regulation framework for the DLP photopolymerization process by combining physics-based modeling, state observation, and nonlinear predictive control. The remainder of this paper is organized as follows. Section 2 establishes a nonlinear state-space model describing the coupled evolution of optical, chemical, thermal, and mechanical fields through a modular modeling approach based on the underlying physical mechanisms. Spatial discretization is further performed to facilitate controller design. Section 3 presents the identification of key model parameters using a self-developed experimental platform, including penetration-depth experiments and ultraviolet differential scanning calorimetry (UV-DSC). An indirect validation method based on heat-flow signals is also proposed to ensure the physical accuracy of the developed model. Section 4 develops a nonlinear model predictive control (NMPC) strategy integrated with a sliding mode observer (SMO) based on the established state-space model. The proposed approach is designed to address the issue of unmeasurable states while achieving stable regulation of the curing process, and the closed-loop stability is proven using the Lyapunov method. Section 5 evaluates the proposed framework through systematic curing experiments and Fourier transform infrared spectroscopy (FTIR) analysis. The performance of the closed-loop control strategy is compared with that of conventional open-loop strategies in terms of curing uniformity enhancement, thereby validating the effectiveness of the proposed framework. Finally, Section 6 summarizes the main conclusions of this study and discusses future research directions. The overall architecture of the proposed framework is illustrated in Fig. 1.

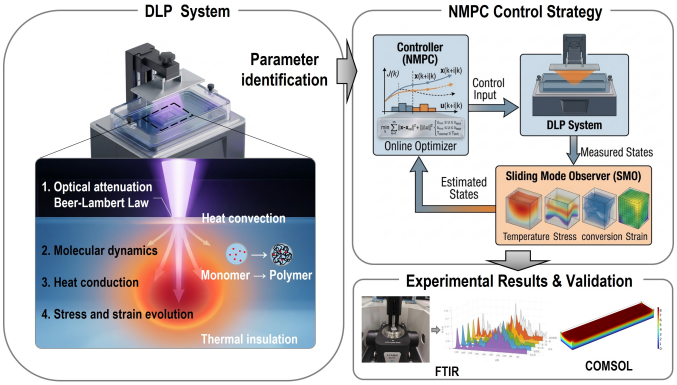


Figure 1. Outline of the Thesis

2. Multiphysics Modeling of the DLP Photopolymerization Process

DLP photopolymerization is a complex coupled process involving optical, chemical, thermal, and mechanical interactions. To systematically characterize its dynamic mechanisms, a modular modeling approach is adopted in this study, where the system is decomposed into four organically interconnected submodels: the irradiation model (Σ_I), kinetic model (Σ_p), heat transfer model (Σ_T), and mechanical evolution model (Σ_M). The overall system can therefore be defined as $\Sigma = \{\Sigma_I, \Sigma_p, \Sigma_T, \Sigma_M\}$, in which bidirectional or unidirectional coupling is realized through

shared state variables among the submodels. To balance computational efficiency and real-time control performance, this study focuses on the single-layer curing process within a one-dimensional spatial domain along the thickness direction (z-direction).

2.1. UV Irradiation and Reaction Kinetics

When ultraviolet (UV) light propagates through a uniformly absorbing medium, part of the optical energy is absorbed and converted into thermal energy, resulting in an exponential attenuation of the transmitted light intensity with increasing penetration depth. The attenuation behavior is positively correlated with both the medium concentration and the penetration depth, and follows the Beer–Lambert law[23]. The attenuation relationship can be expressed as follows:

$$A = \log_{10}\left(\frac{I_0}{I(z)}\right) = \alpha c z \tag{1}$$

where A denotes the absorbance of the medium, I_0 is the incident light intensity, and $I(z)$ represents the light intensity at depth z. The parameter α denotes the molar absorption coefficient, and c is the concentration of the absorbing medium. To simplify the modeling process, the photobleaching effect is neglected. Therefore, for a one-dimensional light attenuation problem with time-varying incident intensity, the light intensity at depth z can be expressed as

$$I(z,t) = \exp\left(-\frac{z}{D_p}\right) I_0(t) \tag{2}$$

where the penetration depth is defined as $D_p = \frac{1}{\ln(10)\alpha c}$, which characterizes the light transmission capability within the medium. The resulting light intensity directly drives the subsequent polymerization reaction.

For the photopolymerization process, previous studies have established reaction kinetics models based on dynamic and isothermal differential scanning calorimetry (DSC) data, where the degree of cure p (i.e., monomer conversion) is treated as the key internal state variable[24]. The general form of the reaction kinetics model is given by

$$\frac{dp}{dt} = r(T) f(p) I^b \tag{3}$$

where $r(T)$ is the temperature-dependent reaction rate constant, and $f(p)$ is a function related to the degree of cure. Its simplest analytical form can be expressed as $f(p) = (1-p)^n$, where n denotes the reaction order.

Under the isothermal assumption, the reaction kinetics equation can be simplified into the following modified form:

$$\frac{\partial p(z,t)}{\partial t} = r(1-p(z,t))^n I(z,t)^b \tag{4}$$

This model characterizes the nonlinear relationship between light intensity and degree of cure, forming the basis for predicting the properties of printed components.

2.2. Heat Transfer Modeling

Photopolymerization is accompanied by significant exothermic reactions and variations in material properties. Based on the law of energy conservation, the one-dimensional heat conduction equation can be expressed as

$$\rho c_p \frac{\partial T(z,t)}{\partial t} = \frac{\partial}{\partial z}\left(k\frac{\partial T(z,t)}{\partial z}\right) + \Delta H_p \frac{\partial p(z,t)}{\partial t} \tag{5}$$

where ρ denotes the material density, c_p is the specific heat capacity, k is the thermal conductivity, and ΔH_p represents the heat of polymerization.

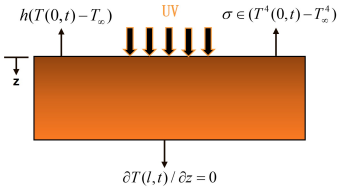


Figure 2. Thermal boundary conditions

The thermal boundary conditions are defined as convective heat transfer at the top surface and thermal insulation at the bottom interface with the substrate, as illustrated in Fig. 2. These boundary conditions can be written as

$$k\frac{\partial T(0,t)}{\partial z} = h(T_\infty - T(0,t)) \quad \frac{\partial T(L,t)}{\partial z} = 0 \tag{6}$$

where T_∞ denotes the ambient temperature.

2.3. Stress–Strain Evolution Modeling

During the photopolymerization process, the increase in monomer conversion leads to significant volumetric shrinkage and progressive variations in mechanical stiffness. To characterize the evolution of mechanical properties after the gelation point, a simplified three-dimensional mechanical model is adopted in this study. As illustrated in Fig. 3, the investigated structure is simplified as a slender body with height L, with emphasis placed on the mechanical behavior along the thickness direction.

According to continuum mechanics theory, the total strain tensor can be decomposed into

$$\varepsilon^{\text{tot}} = \varepsilon^{\text{el}} + \varepsilon^{\text{th}} + \varepsilon^{\text{ch}} \tag{7}$$

where ε^{el} denotes the infinitesimal linear elastic strain tensor, ε^{th} represents the thermally induced strain, and ε^{ch} corresponds to the strain induced by chemical shrinkage.

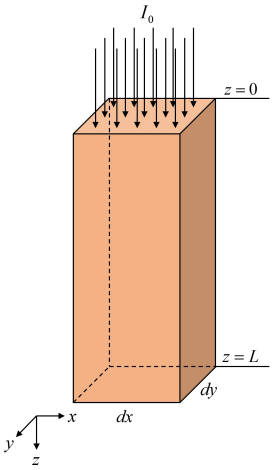


Figure 3. Schematic diagram of the 3D mechanical model

Assuming the material exhibits linear isotropic expansion behavior, the thermal strain can be approximated as a linear function of temperature variation, expressed as

$$\varepsilon^{\mathrm{th}} = \alpha(T - T_0)\mathbf{I} \tag{8}$$

where α is the coefficient of thermal expansion and $\mathbf{I}$ denotes the second-order identity tensor.

Assuming isotropic shrinkage during resin curing, the chemical strain tensor is considered linearly proportional to the degree of cure p. Defining $\varepsilon^{\mathrm{ch}}_{\max}$ as the maximum linear shrinkage strain under fully cured conditions, the chemical strain can be written as

$$\varepsilon^{\mathrm{ch}} = \varepsilon^{\mathrm{ch}}_{\max} p\mathbf{I} \tag{9}$$

For isotropic and homogeneous linear elastic materials, the generalized Hooke's law can be expressed in matrix form as

$$\begin{bmatrix}\sigma_x\\ \sigma_y\\ \sigma_z\\ \tau_x\\ \tau_y\\ \tau_z\end{bmatrix} = \frac{E}{(1+\nu)(1-2\nu)}\begin{bmatrix}1-\nu & \nu & \nu & 0 & \cdots & 0\\ \nu & 1-\nu & \nu & \vdots & \ddots & \vdots\\ \nu & \nu & 1-\nu & 0 & \cdots & 0\\ 0 & \cdots & 0 & \frac{1-2\nu}{2} & 0 & 0\\ \vdots & \ddots & \vdots & 0 & \frac{1-2\nu}{2} & 0\\ 0 & \cdots & 0 & 0 & 0 & \frac{1-2\nu}{2}\end{bmatrix}\begin{bmatrix}\varepsilon_x^{\mathrm{el}}\\ \varepsilon_y^{\mathrm{el}}\\ \varepsilon_z^{\mathrm{el}}\\ \gamma_{xy}\\ \gamma_{xz}\\ \gamma_{yz}\end{bmatrix} \tag{10}$$

where E denotes Young's modulus and ν is Poisson's ratio. The Young's modulus E varies significantly with the degree of cure p. Before the gelation point p_{gel}, the resin behaves as a viscous material with an extremely low modulus, which can be approximated as $E_0 \ll E_{pol}$. After gelation, the modulus gradually increases with the degree of cure until reaching the fully polymerized modulus E_{pol}, which can be represented as $f(p)E_{pol}$. Since the mechanical behavior during the initial curing stage has limited influence on the overall analysis, its uncertainty can be neglected. To ensure computational continuity, a fifth-order polynomial approximation is employed:

$$E_{\mathrm{approx}}(p) = c_0 + c_1 p + c_2 p^2 + c_3 p^3 + c_4 p^4 + c_5 p^5 + \ldots + c_n p^n \tag{11}$$

In this model, the gelation point is set as $p_{gel} = 0.2$, and the fully cured modulus is defined as $E_{pol} = 2$ GPa. The polynomial coefficients are obtained through least-squares fitting. Considering the evolution of material stiffness with the degree of cure p, the overall stiffness tensor can be expressed as $C = E_{\mathrm{approx}}(p)\overline{C}$, where $\overline{C}$ denotes the normalized stiffness matrix and $E_{\mathrm{approx}}(p)$ is the cure-dependent approximate elastic modulus.

According to the boundary constraints, the variables are partitioned into known (k) and unknown (uk) quantities. The stress–strain relationship can therefore be rewritten in block matrix form as

$$\begin{bmatrix}\sigma^{\mathrm{uk}}\\ \sigma^{\mathrm{k}}\end{bmatrix} = E_{\mathrm{approx}}(p)\begin{bmatrix}\overline{C}_{11} & \overline{C}_{12}\\ \overline{C}_{21} & \overline{C}_{22}\end{bmatrix}\begin{bmatrix}\varepsilon^{\mathrm{k}}\\ \varepsilon^{\mathrm{uk}}\end{bmatrix} \tag{12}$$

By rearranging the unknown variables to the left-hand side, the following expression is obtained:

$$\begin{bmatrix}\varepsilon^{\mathrm{uk}}\\ \sigma^{\mathrm{uk}}\end{bmatrix} = \begin{bmatrix}-\overline{C}_{22}^{-1}\overline{C}_{21} & \frac{1}{E_{\mathrm{approx}}(p)}\overline{C}_{22}^{-1}\\ E_{\mathrm{approx}}(p)\left(\overline{C}_{11} - \overline{C}_{12}\overline{C}_{22}^{-1}\overline{C}_{21}\right) & \overline{C}_{12}\overline{C}_{22}^{-1}\end{bmatrix}\begin{bmatrix}\varepsilon^{\mathrm{k}}\\ \sigma^{\mathrm{k}}\end{bmatrix} \tag{13}$$

Thus, the modeling of the Σ_{M} submodule is completed.

2.4. *Integrated Nonlinear State-Space Modeling of the Photopolymerization Process*

To achieve precise regulation of the photopolymerization additive manufacturing process, this section systematically integrates the previously developed optical, chemical kinetic, heat transfer, and curing-induced mechanical submodels into a unified nonlinear state-space formulation.

2.4.1. *Spatial Discretization and Multiphysics Coupling Framework*

The photopolymerization process is governed by a set of coupled partial differential equations (PDEs). To facilitate controller design and numerical implementation, the finite difference method (FDM) is employed to discretize the one-dimensional spatial domain $z \in [0, L]$ with uniform spacing, where the nodal coordinates are defined as $z_i = (i-1)\Delta z$. Through Taylor series expansion, the diffusion term in the temperature field can be transformed into a second-order central difference form, thereby reducing the governing PDE system into a set of ordinary differential equations (ODEs) in both time and space.

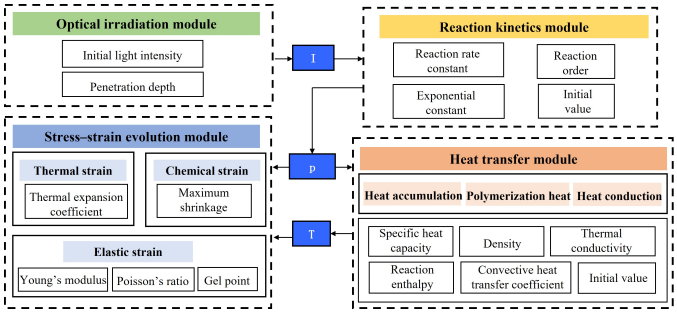


Figure 4. Submodule relationship diagram

The submodules are coupled through shared state variables, as illustrated in Fig. 4. The irradiation intensity I drives the curing reaction, while the exothermic heat generation term (ΔH_p) feeds back into the temperature field. Simultaneously, the evolution of the degree of cure p and temperature T jointly determines the material stiffness $E_{\text{approx}}(p)$ and the resulting residual stress σ.

2.4.2. *Overall Nonlinear State-Space Representation*

In practical single-layer printing scenarios, each material voxel is constrained by the surrounding uncured resin. It can therefore be regarded as a constrained deformation model, where in-plane displacements in the xy plane are restricted, while deformation along the z-direction (thickness direction) is allowed. Based on this physical assumption, the known strain components ε^{k} (driven by chemical shrinkage and thermal expansion) and the unknown quantities ε^{uk}, σ^{uk} can be clearly defined.

The system state vector is defined as

$$\mathbf{x}(t) = \left[p(t),\ \overline{T}(t),\ \varepsilon^{\text{ch}}(t),\ \varepsilon^{\text{th}}(t),\ \varepsilon^{\text{tot}}(t),\ \sigma_{xx,yy}(t)\right]^T, \tag{14}$$

and the control input is given by

$$u(t) = I_0(t)^b. \tag{15}$$

Thus, the state-space equation in the form of

$$\dot{\mathbf{x}}(t) = f(\mathbf{x}(t), u(t)) \tag{16}$$

is obtained:

$$\begin{bmatrix} \dot{p}(t) \\ \dot{\overline{T}}(t) \\ \dot{\varepsilon}^{\text{ch}}(t) \\ \dot{\varepsilon}^{\text{th}}(t) \\ \dot{\varepsilon}^{\text{tot}}_{zz}(t) \\ \dot{\sigma}_{xx,yy}(t) \end{bmatrix} = \begin{bmatrix} g(p(t))u(t) \\ G\overline{T}(t) + jg(p(t))u(t) \\ \varepsilon^{\text{ch}}_{\max} g(p(t))u(t) \\ \alpha G\overline{T}(t) + \alpha jg(p(t))u(t) \\ f_{\varepsilon^{\text{tot}}_{zz}}\left(p(z,t), \dot{p}(z,t)\right) \\ f_{\sigma_{xx,yy}}\left(p(z,t), \dot{p}(z,t), \varepsilon^{\text{ch}}(z,t), \varepsilon^{\text{th}}(z,t)\right) \end{bmatrix} \tag{17}$$

The integrated model not only ensures physical fidelity but also provides an explicit state-space formulation, thereby establishing a theoretical foundation for subsequent shape quality optimization based on model predictive control (MPC).

3. Model Validation and Parameter Identification of Photopolymerization

The experiments in this chapter are conducted on a self-developed bottom-up DLP photopolymerization system. The ultraviolet (UV) light source has a central wavelength of 385 nm, with continuously adjustable light intensity. The primary characterization instrument is an ultraviolet differential scanning calorimeter (UV-DSC), which is used to measure heat flow variations and the evolution of the degree of cure during the photopolymerization process. The experimental material is an acrylate-based photosensitive resin, with a liquid density of 1.1 g/cm^3 and a viscosity of approximately 470 cps.

3.1. *Penetration Depth Parameter Measurement Experiment*

According to the Beer–Lambert law, the ultraviolet energy density $E(z)$ decays exponentially with increasing depth z. When the exposure dose exceeds a critical energy E_c, a phase transition occurs in the resin, and the curing depth C_d satisfies the following relationship[25]:

$$C_d = D_p \ln(E/E_c) \tag{18}$$

The experiments are conducted under three UV intensity levels of 5, 10, and 20 mW/cm^2. For each intensity, exposure times of 0.5 s, 1 s, 2 s, and 3 s are applied. The resulting cured layer thickness is measured for each sample (see Fig. 5), and the penetration depth D_p and critical exposure energy E_c are obtained through curve fitting.

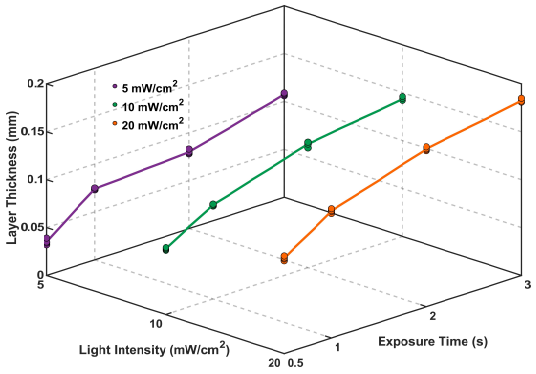


Figure 5. Measured data of printed layer thickness

Nonlinear least squares fitting is performed (Fig. 6), and the identified parameters are $D_p = 0.0455$ mm and $E_c = 1.1827$ mJ·cm^{-2}. These parameters characterize the UV absorption behavior of the resin as well as the threshold energy required for the onset of polymerization.

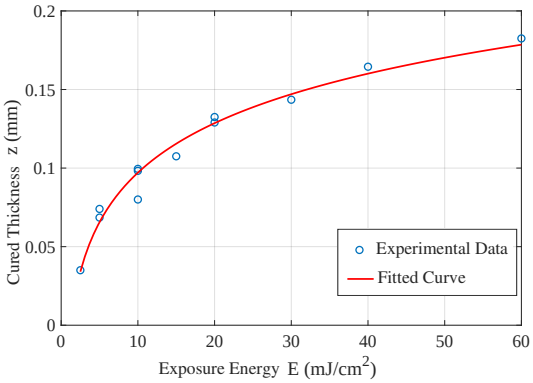


Figure 6. Curve fitting results of experimental data

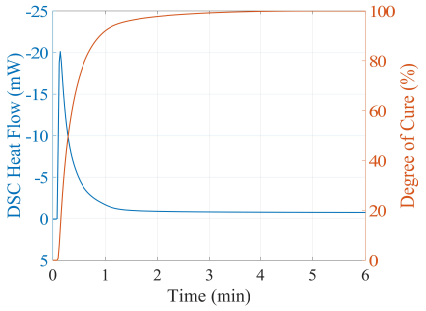
3.2. *Reaction Heat Measurement Experiment Based on Isothermal DSC*

Isothermal UV-DSC is employed to monitor the heat flow of the photopolymerization process under a nitrogen atmosphere

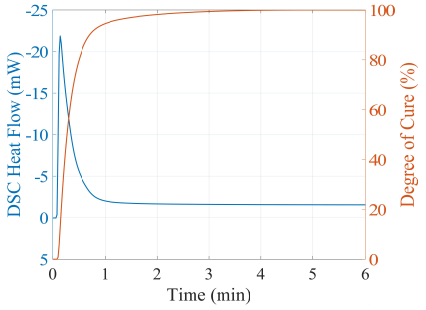
at 25°C. The reaction enthalpy change ΔH and the instantaneous degree of cure $p(t)$ are calculated as follows[26]:

$$\Delta H = \frac{\int q(t)dt}{m}, \quad p(t) = \frac{\int_0^t q(\tau)d\tau}{\int_0^{t_{end}} q(\tau)d\tau} = \frac{Q(t)}{Q_\infty} \tag{19}$$

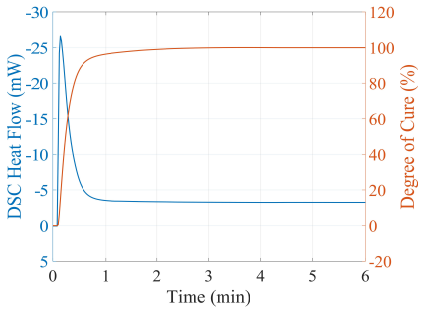
where $q(t)$ is the heat flow signal and m is the sample mass.



(a) 5 mW/cm^2



(b) 10 mW/cm^2



(c) 20 mW/cm^2

Figure 7. Evolution of DSC heat flow and degree of cure over time

The experimentally measured average reaction enthalpy is 331.2 J/g (equivalently 0.36432 GJ/m^3). The heat flow and degree of cure curves under different light intensities are shown in Fig. 7. An n-order kinetic model is used for inverse parameter identification, yielding $r = 0.0385$, $n = 1.2396$, and $b = 0.4657$. The coefficient of determination is $R^2 = 0.9964$, indicating that the proposed model accurately captures the autoacceleration behavior of the photopolymerization process.

3.3. Chemical Shrinkage Measurement Experiment

Standard cubic specimens with dimensions of 15 × 15 × 3.5 mm were fabricated and their geometrical dimensions were measured after curing (Table 1). The average volumetric chemical shrinkage was calculated as $\varepsilon_{ch,vol} \approx -0.0185$. This parameter establishes the baseline eigenstrain induced by chemical reactions in the mechanical model.

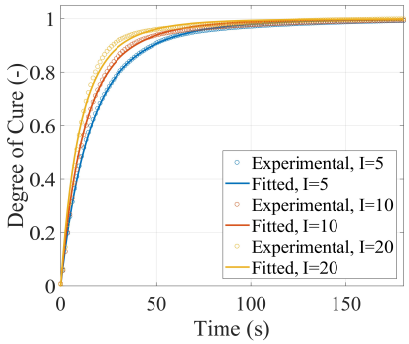


Figure 8. Fitting of the curing kinetic model

Table 1: Measured geometric dimensions of the specimens

Sample No.	Length (mm)	Width (mm)	Thickness (mm)
1	14.892	14.920	3.478
2	14.887	14.913	3.477
3	14.929	14.904	3.481
4	14.874	14.912	3.474
5	14.885	14.978	3.485
6	14.880	14.911	3.476

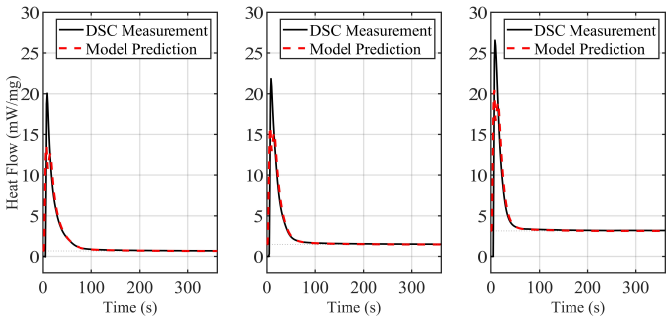
3.4. Heat Transfer Model Validation

To validate the thermodynamic module, a non-isothermal UV-DSC experiment is conducted. Since the physical model computes reaction heat generation at a microscopic idealized level, whereas the DSC experiment captures heat flow signals via macroscopic sensors, systematic discrepancies exist between the two. Therefore, a capture factor η and a baseline offset O_{offset} are introduced to construct a mapping between the theoretical predicted heat flow HF_{sim} and the experimentally measured signal:

$$HF_{sim}(t) = \eta\left[\frac{1}{\rho}\left(\Delta H_p \frac{\partial p}{\partial t} - \rho c_p \frac{\partial \overline{T}}{\partial t}\right)\right] + O_{offset} \tag{20}$$

This expression reflects the energy competition mechanism between chemical exothermic heat generation and sensible heat storage.

By comparing the experimental and simulated results under different light intensities (Fig. 9), the model demonstrates good predictive capability over the entire reaction process, with an overall coefficient of determination of $R^2 = 0.9597$ (Table 2). As the light intensity increases, the rise in O_{offset} reflects the influence of radiative thermal loading on the baseline signal, thereby validating the physical consistency of the thermo-kinetic coupling formulation.



(a) 5 mW/cm^2 (b) 10 mW/cm^2 (c) 20 mW/cm^2

Figure 9. Comparison between experimental and simulated heat flow

Table 2: Thermal Model Fitting Parameters and Errors under Different Light Intensities

Light Intensity (mW/cm^2)	Goodness of Fit (R^2)	RMSE (mW/mg)	Capture Factor (η)	Baseline Offset (O_{offset})
5	0.9568	0.4847	0.001078	0.6716
10	0.9623	0.5151	0.001118	1.4789
20	0.9449	0.6937	0.001140	3.1445

4. Model Predictive Control System Design

The continuous photopolymerization process involves monomer conversion, exothermic reactions, and interlayer mechanical evolution, exhibiting strong nonlinearity, time-varying behavior, and tightly coupled multiphysics interactions. Conventional PID or linear control strategies are insufficient to achieve accurate degree-of-cure tracking while simultaneously satisfying physical constraints such as light intensity limits and thermal stress thresholds. Based on the state-space model established in Chapter 2, this chapter proposes a closed-loop control framework integrating nonlinear model predictive control (NMPC) with a sliding mode observer (SMO). To further improve real-time computational efficiency under complex process conditions, a multilayer perceptron (MLP) is introduced to construct a data-driven surrogate predictive controller.

4.1. Nonlinear Model Predictive Controller Design

Consider the discrete-time nonlinear system model:

$$\begin{cases} x(k+1) = f(x(k), u(k)) \\ y(k) = h(x(k)) \end{cases} \tag{21}$$

For a three-layer discretized model with $N = 3$, the system dimension is 18. In order to track the reference degree-of-cure trajectory $r(k)$ while minimizing energy consumption and ensuring smooth control actions, the following cost function is formulated:

$$\begin{aligned} \min_{u(k)} J(k) = & \frac{1}{2} \sum_{i=0}^{N_p-1} \Big(\|x(k+i|k) - x_{\text{ref}}(k+i)\|_Q^2 \\ & + \|u(k+i|k)\|_R^2 \\ & + \|\Delta u(k+i|k)\|_P^2 \Big) \\ & + \frac{1}{2} \|x(k+N_p|k) - x_{\text{ref}}(k+N_p)\|_{Q_N}^2 \end{aligned} \tag{22}$$

where Q is the state tracking weighting matrix, R is the control effort weighting matrix, and P is the increment weighting matrix used to suppress control chattering. At each sampling instant, the optimal control sequence U_k is obtained by solving a nonlinear programming problem, and only the first control input $u(k)$ is implemented according to the receding horizon strategy of model predictive control.

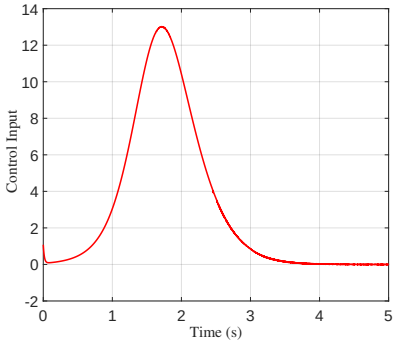


Figure 10. Optimal control input trajectories of NMPC

Fig. 11 compares the performance of NMPC, GS-PID, and LQR under a step reference trajectory. Quantitative results show that NMPC improves the tracking accuracy of the degree of cure by 16.38% compared with LQR. More importantly, NMPC exhibits strong predictive behavior: before the step change at $t = 1.0$ s, the control input u responds in advance (see Fig. 10), effectively mitigating the typical delay observed in conventional PID controllers.

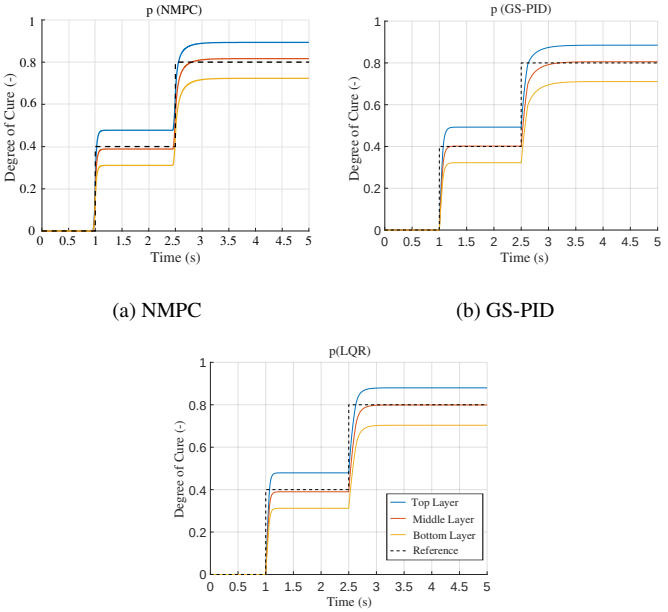
4.2. Sliding Mode Observer Design

In practical DLP scenarios, only the surface temperature and degree of cure can be measured using infrared and spectroscopic sensors, while internal stress and strain states are unobservable. To achieve full-state feedback, the following sliding mode observer is constructed:

$$\begin{aligned} \dot{\hat{x}} &= f(\hat{x}, u) + H^T L_s \Phi(e) \\ e &= y - \hat{y} = y - H\hat{x} \end{aligned} \tag{23}$$

The switching term $\Phi(e)$ is implemented using a continuous hyperbolic tangent function to eliminate high-frequency chattering:

$$\Phi(e) = \tanh\left(\frac{y - H\hat{x}}{\epsilon}\right) \tag{24}$$



(a) NMPC (b) GS-PID

(c) LQR

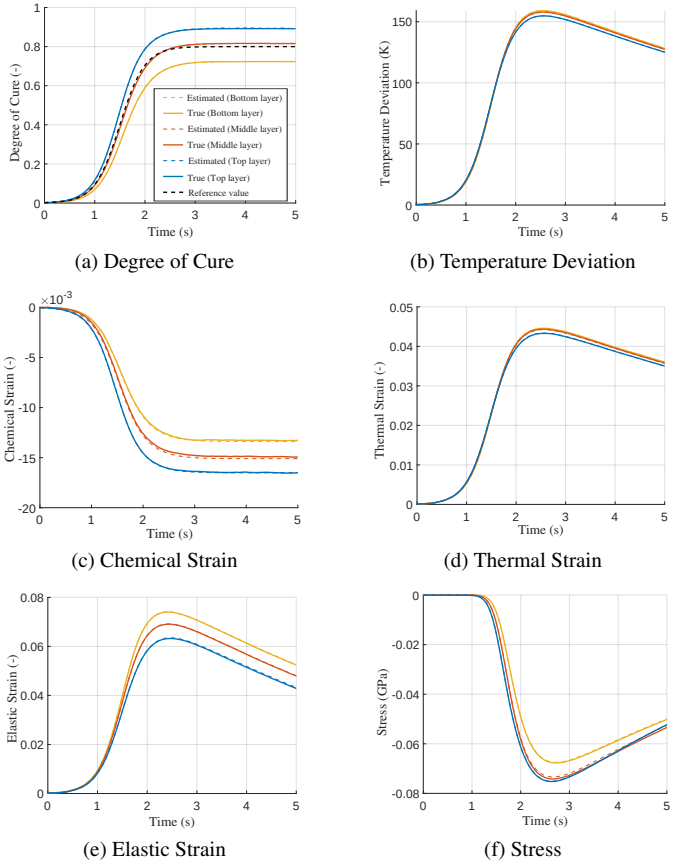
Figure 11. Comparison of degree-of-cure tracking performance under different control strategies

The gain matrix L_s is designed to satisfy the Lyapunov stability criterion such that the estimation error satisfies $\dot{V} = e^T \dot{e} < 0$, ensuring that the estimated states converge to the true state manifold in finite time.

To verify the robustness of the SMO, process noise following a Gaussian distribution $w \sim \mathcal{N}(0, W)$ and measurement noise $v \sim \mathcal{N}(0, V)$ are introduced in the simulation. The covariance matrix W reflects a 1–10% uncertainty in the model parameters. The reference trajectory is defined as an S-shaped curve of the degree of cure. For this reference trajectory, the SMO simulation results are shown in Fig. 12.

From the evolution curves of the six state variables in Fig. 12, it can be observed that the proposed NMPC+SMO-based control strategy exhibits excellent state tracking and estimation performance throughout the entire curing process. The estimated states provided by the sliding mode observer (dashed lines) closely match the true system states (solid lines), demonstrating fast convergence and accurate state reconstruction under strong nonlinearity and multiphysics coupling conditions. This effectively suppresses model uncertainties and external disturbances. Moreover, the proposed approach clearly distinguishes the state evolution across different depth layers and enables coordinated regulation, thereby validating the effectiveness and robustness of the control framework for tracking in complex multiphysics coupled systems. The estimation errors of the six state variables are shown in Fig. 13.

As shown in Table 3, the SMO achieves a reconstruction RMSE of 6.4×10^{-4} GPa for the residual stress, with a relative error of only 0.85%, demonstrating its capability to provide high-quality feedback signals under complex disturbance conditions.

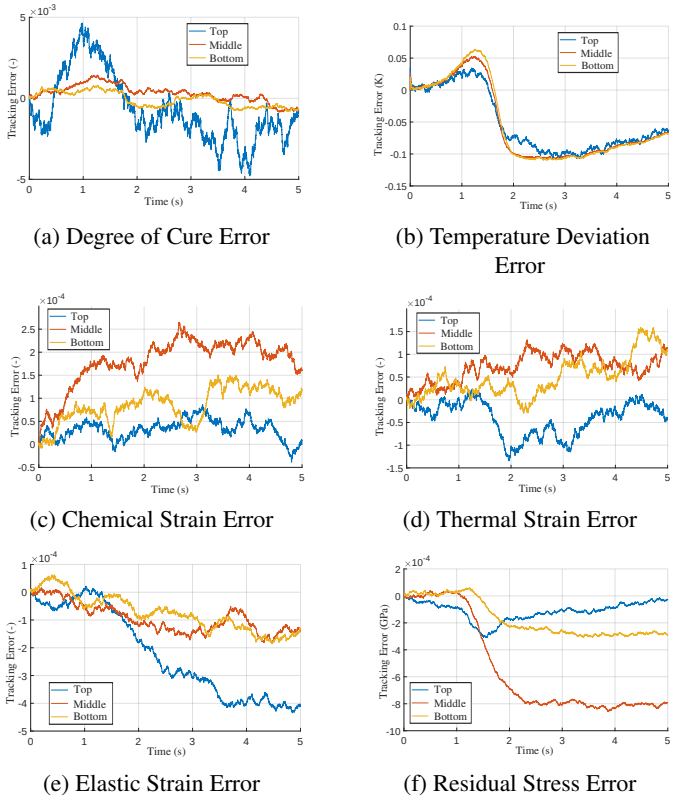


(a) Degree of Cure (b) Temperature Deviation

(c) Chemical Strain (d) Thermal Strain

(e) Elastic Strain (f) Stress

Figure 12. Comparison between estimated and actual state variables



(a) Degree of Cure Error (b) Temperature Deviation Error

(c) Chemical Strain Error (d) Thermal Strain Error

(e) Elastic Strain Error (f) Residual Stress Error

Figure 13. Estimation Errors of State Variables ($x - \hat{x}$)

Table 3: Statistical Analysis of Estimation Errors for Physical Quantities

Physical Quantity	FSR	RMSE	Relative Error
Degree of Cure (p)	$0 \sim 1.0$	2.2×10^{-3}	0.22%
Temperature Rise (ΔT)	$0 \sim 160$ K	7.9×10^{-2} K	0.05%
Chemical Strain ($\varepsilon_{\mathrm{ch}}$)	$0 \sim 0.017$	1.9×10^{-4}	1.12%
Thermal Strain ($\varepsilon_{\mathrm{th}}$)	$0 \sim 0.045$	7.8×10^{-5}	0.17%
Total Strain (ε_{zz})	$0 \sim 0.075$	2.7×10^{-4}	0.36%
Stress (σ)	$0 \sim 0.075$ GPa	6.4×10^{-4} GPa	0.85%

4.3. Integration and Training of Neural Network-Based Prediction Algorithm

Although NMPC exhibits superior performance, the computational complexity of solving nonlinear programming problems online increases exponentially with the prediction horizon N_p, making it difficult to satisfy real-time control requirements. To address this issue, this chapter adopts a strategy in which "NMPC generates data and an MLP learns offline" to construct an approximate controller.

The input vector at time step k is defined to include the current estimated state and the reference trajectory sequence over the prediction horizon:

$$X_{input}(k) = \left[\hat{X}(k);\ x_d(k); \ldots;\ x_d(k+M)\right] \in \mathbb{R}^{18+18(M+1)} \quad (25)$$

where $\hat{X}(k)$ denotes the historical sequence of estimated states, and x_d represents the reference value. In this study, $M = 5$ is selected.

A four-layer feedforward neural network structure (126-128-128-64-1) is adopted. The hyperbolic tangent function (tansig) is used as the activation function in hidden layers to capture the nonlinear characteristics of the physical system. To eliminate the effect of scale differences and prevent gradient vanishing, both input and output data are normalized to the interval $[-1, 1]$. The network is trained using the Levenberg–Marquardt second-order optimization algorithm. The loss function is defined as the mean squared error (MSE) between the predicted control input $\hat{U}(k)$ and the optimal NMPC control input $U_{\mathrm{opt}}(k)$:

$$J = \frac{1}{N}\sum_{k=1}^{N}(U_{opt}(k) - \hat{U}(k))^2 \quad (26)$$

After 500 iterations, the MSE loss decreases to 0.0002, and the residual distribution exhibits a typical Gaussian characteristic, indicating that the neural network has successfully learned the implicit control law of NMPC. The trained function $u = f(x_d, \hat{x})$ is then embedded into Simulink according to the logical structure shown in Fig. 14.

Based on this implementation, a step-type reference trajectory is used as a validation case. The comparison results of the predicted control inputs are shown in Fig. 15.

Regarding the degree of cure, which is a key state variable, its dynamic tracking performance is shown in Fig. 16.

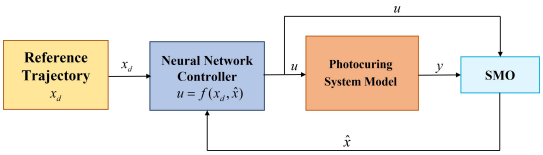


Figure 14. Simulink structure of the MLP-based control function

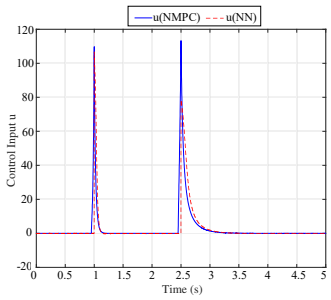


Figure 15. Comparison of NN-predicted control inputs

As shown in Fig. 16, the NN-predicted trajectories for the bottom, middle, and top layers are all able to successfully follow the step changes in the reference trajectory. The overall trend is highly consistent with that of NMPC, and the controller responds correctly to both step inputs, enabling the system to reach the desired trajectory.

5. Experimental Validation and Multiphysics Simulation

To verify the feasibility and effectiveness of the proposed control strategy in an actual DLP photopolymerization process, this study conducts experimental and simulation validations from four aspects: controllability of the control inputs, consistency of curing behavior, improvement of interlayer uniformity, and rationality of multiphysics responses. Unlike conventional process studies that focus solely on final curing depth or geometric accuracy, this work emphasizes the regulation capability of control inputs on the curing kinetics, as well as the consistency between model predictions and actual material responses. Due to limitations in the current experimental setup, a real-time closed-loop feedback system was not implemented in the experimental stage. Instead, an "offline optimization–open-loop implementation–offline characterization" validation framework is adopted. First, the optimal light-intensity time sequence is generated by the proposed controller. Then, this input is discretized and applied to the actual DLP photopolymerization platform. Finally, Fourier transform infrared spectroscopy (FTIR) measurements and COMSOL multiphysics simulations are used to comprehensively evaluate the curing behavior and the coupled thermal–mechanical responses.

5.1. Experimental Validation of Curing Behavior

The experimental platform is based on a self-built DLP photopolymerization system with adjustable exposure intensity output, which enables the implementation of non-constant light intensity inputs. A commercially available ABS-type photosensitive resin is used as the experimental material. To verify the

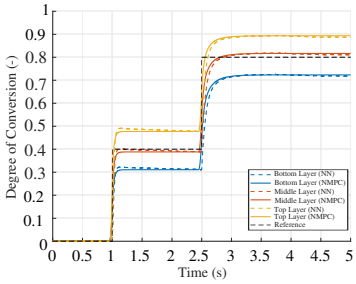


Figure 16. Comparison of degree of cure

regulatory effect of control inputs on curing behavior, Fourier transform infrared spectroscopy (FTIR) is employed to perform offline measurements and analysis of the degree of cure under different exposure conditions.

The experimental procedure is as follows: first, the optimal light-intensity time sequence is generated offline by the controller based on the kinetic model; second, the continuous control signal is converted into a stepwise discretized light-intensity sequence executable by the experimental system; third, samples are fabricated under identical geometric dimensions and process boundary conditions; finally, attenuated total reflectance FTIR (ATR-FTIR) is used to quantitatively characterize the curing states at both the top and bottom surfaces of the samples, and the thermo-mechanical consistency is further analyzed in conjunction with multiphysics simulations.

5.1.1. Sample Preparation and Curing Experiment

The continuous light-intensity profile is segmented along the time axis and converted into a stepwise input based on an equivalent energy principle to facilitate experimental implementation. The resulting profile is shown as follows:

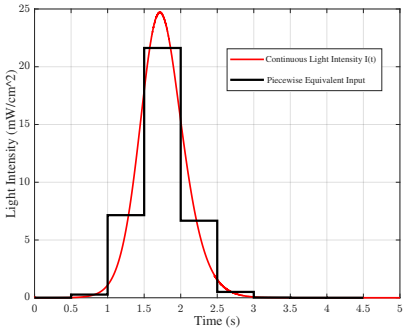


Figure 17. Comparison between continuous and discrete light intensity inputs

During the sample preparation stage, single-layer exposure specimens are designed for curing behavior validation. The specimen geometry is set as 15 mm × 15 mm × 50 μm, and three parallel samples are fabricated under each exposure condition to improve statistical reliability. Multiple exposure conditions are designed in the experiments. The low-energy input group, due to being close to the gelation threshold, fails to form stable structures and is therefore excluded from subsequent degree-of-cure analysis. The remaining samples are cleaned with ethanol and dried prior to FTIR characterization.

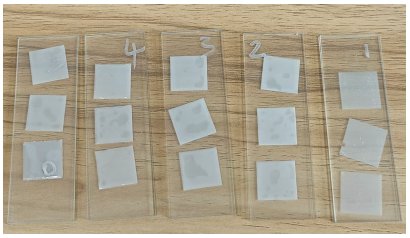


Figure 18. 3D printed sample

5.1.2. Quantitative Analysis of Degree of Cure Based on FTIR

To evaluate the curing behavior under different exposure inputs, attenuated total reflectance Fourier transform infrared spectroscopy (ATR-FTIR) is employed to perform offline measurements on both the top and bottom surfaces of the samples, and the degree of cure is quantitatively calculated based on characteristic peak variations, as shown in Fig. 19. For the acrylate-based resin system used in this study, the absorption peak at approximately 1635 cm^{-1} corresponds to the C=C stretching vibration, whose intensity gradually decreases as the polymerization reaction proceeds. The absorption peak at approximately 1720 cm^{-1} corresponds to the C=O group, which remains relatively stable during the reaction and is therefore used as an internal reference for normalization.

To reduce the influence of sample thickness, contact pressure, and measurement conditions, the peak area ratio method is adopted to calculate the degree of cure. The normalized characteristic peak ratio for the i-th sample is defined as:

$$r_{pA}(i) = \frac{A_{\mathrm{rxn}}(i)}{A_{\mathrm{ref}}(i)} \tag{27}$$

where $A_{\mathrm{rxn}}(i)$ denotes the area of the reactive characteristic peak, and $A_{\mathrm{ref}}(i)$ represents the area of the reference peak. The degree of cure can then be expressed as

$$p(i) = \left(1 - \frac{r_{pA}(i)}{r_{pA,0}}\right) \times 100\% \tag{28}$$

where $r_{pA,0}$ is the initial peak area ratio of the uncured sample.



(a) Liquid resin measurement (b) Printed sample measurement

Figure 19. FTIR measurement setup and sample characterization

In addition to the C=C characteristic peak, this study further introduces the =C–H characteristic peak for cross-validation of

the curing process, thereby improving the robustness and reliability of the results. The FTIR spectra of different samples indicate that with increasing exposure time, the intensity of the reactive characteristic peaks continuously decreases, while the reference peak remains relatively stable. This behavior confirms that significant polymerization conversion occurs in the resin system.

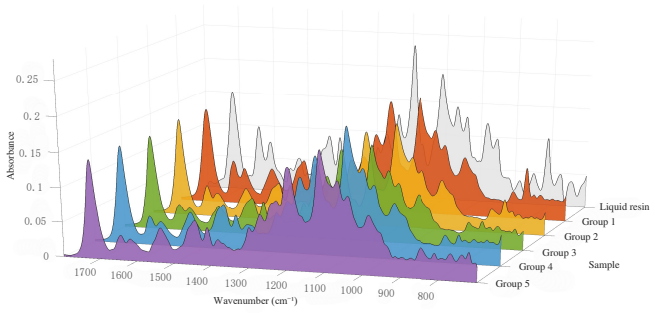


Figure 20. FTIR absorbance spectra

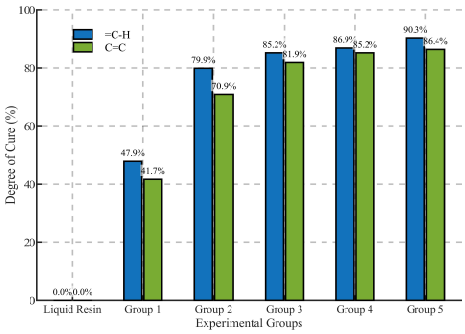


Figure 21. Comparison of degree of cure calculation results

From the evolution of the degree of cure, it can be observed that the samples exhibit a pronounced rapid crosslinking behavior at the initial irradiation stage, during which the degree of cure increases sharply. As the polymer network gradually forms, diffusion constraints within the system become increasingly significant, leading to a progressive reduction in the curing rate until it eventually approaches a plateau. The experimental results show that the final degree of cure at the top layer reaches approximately 85%–95%, while that at the bottom layer is about 60%–80%. This result is consistent with the physical law of light intensity attenuation along the thickness direction within the resin.

As shown in Fig. 22 and Fig. 23, a further comparison between the experimental mean values (with standard deviation) and the numerical model predictions is conducted. It can be observed that, regardless of whether the degree of cure is calculated based on the C=C or the =C–H characteristic peaks, the evolution trends of curing at both the top and bottom layers are in good agreement with the model predictions.

Overall, the FTIR experimental results demonstrate that the proposed control inputs can be stably implemented in a real photopolymerization system. Moreover, the model accurately

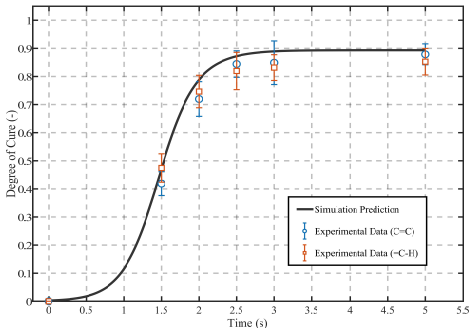


Figure 22. Comparison of experimental statistical data and simulation results (Top Layer)

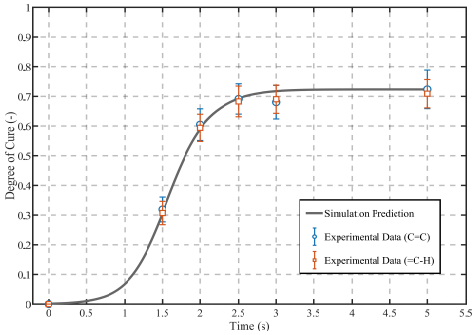


Figure 23. Comparison of experimental statistical data and simulation results (Bottom Layer)

predicts the evolution of the curing behavior along the thickness direction, thereby validating the correctness of both the kinetic model and the control input design.

5.1.3. Comparison Between Variable and Constant Light Intensity Exposure

To further evaluate the effectiveness of the proposed variable light-intensity strategy in improving curing uniformity along the thickness direction, a constant light-intensity exposure strategy with equivalent total energy is introduced as a benchmark. The equivalent constant intensity is defined based on the principle of identical total exposure dose with the variable light-intensity input, i.e.,

$$I_{\text{eq}} = \frac{1}{t_{\max}} \int_0^{t_{\max}} I(t)\,\mathrm{d}t \tag{29}$$

where $I(t)$ denotes the time-varying light intensity input, and $t_{\max}$ is the total exposure time.

Under identical resin material, sample geometry, and total exposure energy conditions, the samples fabricated using the two exposure strategies are tested for the degree of cure at both the top and bottom layers. The experimental results are presented in Table 4 and Fig. 24.

The results indicate that, under equivalent total energy conditions, the constant light-intensity exposure strategy leads to insufficient energy delivery in the bottom layer due to the attenuation of UV light within the resin, resulting in a lower degree of cure at the bottom and a larger interlayer discrepancy. In

Table 4: Cure Uniformity Comparison

Strategy	Layer	Mean ± Std (%)	Δp	Improve.
Const.	Top	87.62 ± 2.61	19.40	–
	Bottom	68.22 ± 2.83		
Var.	Top	87.97 ± 1.79	15.17	21.80%
	Bottom	72.80 ± 3.86		

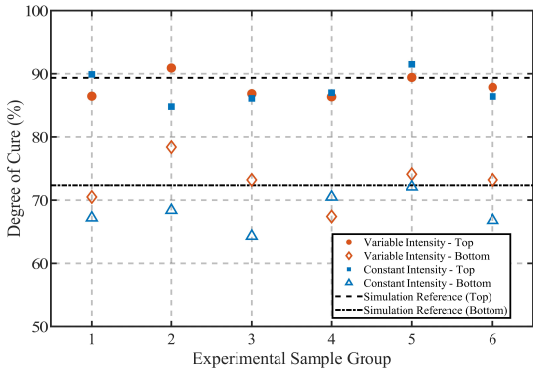


Figure 24. Comparison of cure degree under constant and NMPC-Controlled light intensity

contrast, the variable light-intensity strategy dynamically adjusts the light distribution during critical curing stages, thereby improving effective energy utilization in deeper regions at later stages of the process. As a result, the bottom-layer degree of cure increases from 68.22% to 72.80%, while the interlayer curing difference decreases from 19.40% to 15.17%, corresponding to an improvement in uniformity of approximately 21.80%.

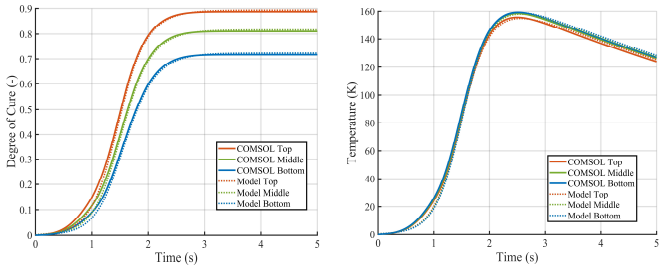
These results demonstrate that the proposed control strategy not only achieves effective tracking of the desired curing trajectory, but also exhibits clear advantages over conventional constant-intensity strategies in enhancing curing uniformity along the thickness direction.

5.2. COMSOL Multiphysics Simulation Validation

To further verify the physical consistency of the proposed model and control inputs at the thermo-mechanical level, a multiphysics coupling simulation model is developed in COMSOL Multiphysics, incorporating light transport, curing kinetics, heat transfer, and solid mechanics. The model takes the optimal light-intensity sequence generated by the controller as the external input and simulates the evolution of the degree-of-cure field, temperature field, and the mechanical response induced by shrinkage and thermal effects during the curing process.

5.2.1. Consistency Analysis of Degree of Cure and Temperature Fields

Under identical light-intensity input conditions, the results predicted by the control model are compared with those obtained from high-fidelity COMSOL simulations in terms of the evolution of the degree of cure and temperature at different thickness positions.



(a) Degree of cure (b) Temperature deviation

Figure 25. Comparison between COMSOL and the proposed model

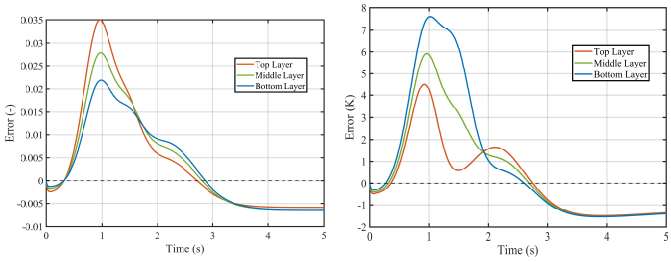
Overall, the control model is able to accurately reproduce the dynamic evolution trends of both the degree of cure and temperature. To quantitatively evaluate the consistency, the root mean square error (RMSE) is adopted to statistically assess the results at different layer positions, as shown in Table 5.

Table 5: RMSE of Cure Degree and Temperature

Layer	Cure RMSE	Temp. RMSE (K)
Top	0.0128	1.6792
Middle	0.0112	2.3024
Bottom	0.0097	3.2056

It can be observed that the RMSE of the degree of cure at all three layer positions is on the order of 10^{-2}, indicating that the control model achieves high accuracy in predicting curing kinetics. The temperature prediction error is slightly larger; however, it remains within an acceptable range. Moreover, the error is mainly concentrated near the bottom boundary region, which is attributed to the stronger exothermic reaction and higher sensitivity to boundary conditions in this area.

Further spatiotemporal error analysis shows that no significant cumulative deviation or instability is observed in either the degree of cure or temperature predictions. This indicates that the proposed model can reliably capture the typical opto-thermal-chemical coupled dynamics in the DLP photopolymerization process.



(a) Cure degree error (b) Temperature error

Figure 26. Spatio-Temporal Error Distribution

5.2.2. Analysis of stress and warpage Response

Based on the thermo-chemical response validation, this section further investigates the mechanical response evolution under the proposed control inputs. COMSOL simulation results

indicate that curing-induced shrinkage and reaction heat jointly lead to the development of non-uniform residual stresses within the material. The stress magnitude accumulates rapidly during the curing process and gradually relaxes in the later stage of exposure.

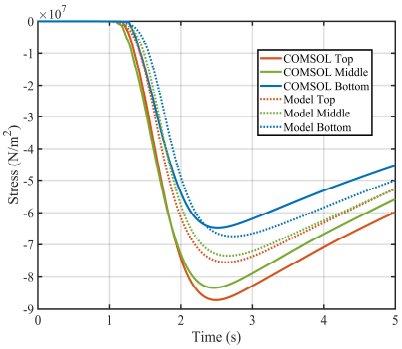
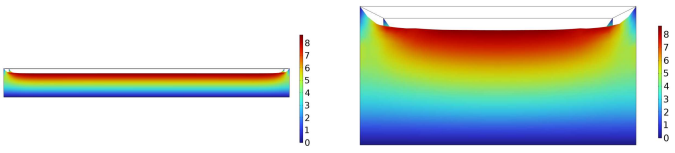


Figure 27. Comparison of residual stress state

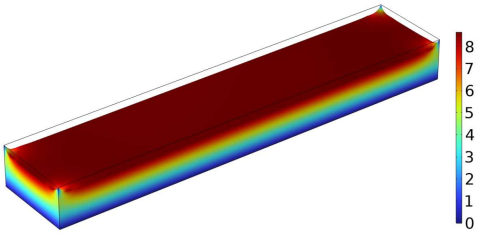
From the through-thickness distribution, the bottom layer exhibits a higher stress level compared to the middle and top layers, due to its earlier solidification and stronger substrate constraint. This behavior is consistent with the stress formation mechanism in photopolymerization, which is jointly governed by boundary constraints and the curing sequence.

Furthermore, after releasing the bottom constraint, the warpage deformation of the specimen is analyzed. A typical edge-up and center-shrink deformation pattern is observed, indicating that non-uniform curing along the thickness direction can further translate into geometric distortion risks at the structural scale.



(a) XZ-plane deformation contour

(b) YZ-plane deformation contour



(c) Overall 3D warpage deformation of the specimen

Figure 28. Residual-stress-induced warpage deformation after release of specimen constraints

To quantitatively evaluate the consistency of stress prediction, the coefficient of determination (R^2), normalized root mean square error (NRMSE), and RMSE are further adopted to statistically analyze the stress results at different layer positions, as shown in Table 6. The results indicate that the model achieves high prediction accuracy for stress evolution in the top and middle layers, while relatively larger errors are observed in the bottom layer. This discrepancy is mainly attributed to the high sensitivity of local stress responses to numerical settings under fixed boundary conditions. Nevertheless, the model is still able to accurately capture the overall temporal evolution and through-thickness distribution characteristics of the stress field.

Table 6: Stress Simulation Error Metrics

Layer	R^2	NRMSE (%)	RMSE (MPa)
Top	0.9295	10.55	7.96
Middle	0.9205	11.36	8.35
Bottom	0.7143	21.87	14.76

Overall, the multiphysics simulation results further demonstrate that the proposed control inputs can effectively regulate the chemical curing behavior, while the induced temperature field, stress field, and final warpage trends all exhibit good physical consistency and rationality.

6. Conclusion and Future Work

The photopolymerization additive manufacturing process involves the deep coupling of multiple physical mechanisms, including optical attenuation, chemical polymerization, heat transfer, and mechanical evolution. Its strong nonlinearity and dynamic complexity pose significant challenges for high-precision control. Focusing on the digital light processing (DLP) process, this study systematically develops an end-to-end research framework covering mechanistic modeling, key parameter identification, and advanced control algorithm design, thereby establishing a physically consistent and practically implementable control system. The main conclusions are summarized as follows:

(1) A multiphysics-coupled mechanistic model with parameter identification was established. Based on UV light propagation theory, free-radical polymerization kinetics, energy conservation in heat conduction, and generalized Hooke's law, the multiphysics evolution process was theoretically formulated. A quantitative relationship between energy input and curing depth was derived. The polymerization kinetic model was validated via UV-DSC experiments, and an energy conservation-based mapping between microscale reaction heat and macroscopic heat flow signals was established, providing a reliable basis for temperature field prediction.

(2) A state-space representation of the complex system was developed. Through spatial discretization, the coupled partial differential equations were transformed into a nonlinear state-space model, integrating thermal expansion and chemical shrinkage mechanisms, thereby providing a unified mathematical framework for real-time control design.

(3) An intelligent closed-loop control strategy was proposed. A regulation architecture combining a sliding mode observer

(SMO) and nonlinear model predictive control (NMPC) was constructed. By incorporating a neural network-based approximation scheme, the online computational efficiency was significantly improved, and FTIR experiments verified that the curing trajectory can closely follow the prescribed reference profile.

(4) The forming quality and interlayer uniformity were significantly improved. Experimental results show that the proposed variable light-intensity strategy improves interlayer curing uniformity by 21.80% compared with conventional constant-intensity strategies, demonstrating the superiority of multiphysics coupled regulation.

Although this study achieves promising results in single-layer curing control, several limitations remain due to experimental constraints and model complexity. Future work will focus on developing a real-time closed-loop experimental platform with in-situ state feedback, potentially enabled by infrared thermography or ultrasonic sensing techniques for online error correction. In addition, the modeling framework will be extended from pure resin systems to high-solid-loading slurries containing ceramic or metallic particles, to investigate control strategies under complex scattering mechanisms. Furthermore, the scope will be expanded from single-layer curing to multi-layer continuous printing processes, with particular attention to cumulative thermal effects and interlayer stress redistribution during long-duration fabrication. By establishing long-horizon evolution models, issues such as warpage and dimensional instability in large-scale complex structures can be addressed, ultimately advancing photopolymerization control technologies toward higher levels of industrial application.

Acknowledgments

This work was supported by the National Natural Science Foundation of China(Grant Nos.52275372, U24B2053,52405411), the Natural Science Basic Research Program of Shaanxi (Grant No. 2025JC-YBQN-543), and the China Postdoctoral Science Foundation (2025M771324).

References

[1] I. Rodriguez-Conde, C. Campos, Towards customer-centric additive manufacturing: Making human-centered 3d design tools through a handheld-based multi-touch user interface, Sensors 20 (15) (2020) 4255.

[2] G. Liu, X. Zhang, X. Chen, Y. He, L. Cheng, M. Huo, J. Yin, F. Hao, S. Chen, P. Wang, et al., Additive manufacturing of structural materials, Materials Science and Engineering: R: Reports 145 (2021) 100596.

[3] J. Zhao, Q. Li, F. Jin, N. He, Digital light processing 3d printing kevlar composites based on dual curing resin, Additive Manufacturing 41 (2021) 101962.

[4] L. Yue, S. Macrae Montgomery, X. Sun, L. Yu, Y. Song, T. Nomura, M. Tanaka, H. Jerry Qi, Single-vat single-cure grayscale digital light processing 3d printing of materials with large property difference and high stretchability, Nature communications 14 (1) (2023) 1251.

[5] W. Xiang, P. Xiangtao, S. Peng, H. Wen-hao, Monte carlo simulation model of micro light beam solidification, Acta Optica Sinica 28 (2008) 2388–2393.

[6] K. Gao, B. Ingenhut, A. Van De Ven, F. V. Mackenzie, A. ten Cate, Multiphysics modelling of photopolymerization in stereolithography printing process and validation, in: Proceedings of the 2018 COMSOL Conference in Lausanne, Lausanne, Switzerland, 2018, pp. 22–24.

[7] T. Tang, N. Gopalabhatla, J. Seelapureddy, J. Westerham, S. A. Remani, S. M. A. Nipu, M. Yoo, S. Guo, X. Li, Enhancing polymer composite performance through optimized alignment with machine learning and in-situ monitoring in electrically assisted vat photopolymerization, Composites Science and Technology 276 (2026) 111506.

[8] M. M. Emami, D. W. Rosen, Modeling of light field effect in deep vat polymerization for grayscale lithography application, Additive Manufacturing 36 (2020) 101595.

[9] M. Par, P. Burrer, K. Prskalo, S. Schmid, A.-L. Schubiger, D. Marovic, Z. Tarle, T. Attin, T. T. Tauböck, Polymerization kinetics and development of polymerization shrinkage stress in rapid high-intensity light-curing, Polymers 14 (16) (2022) 3296.

[10] I. Valizadeh, T. Tayyarian, O. Weeger, Influence of process parameters on geometric and elasto-visco-plastic material properties in vat photopolymerization, Additive Manufacturing 72 (2023) 103641.

[11] Y. Xiang, C. Schilling, N. Arora, A. Boydston, S. Rudykh, Mechanical characterization and constitutive modeling of visco-hyperelasticity of photocured polymers, Additive Manufacturing 36 (2020) 101511.

[12] F. Petko, A. Świeży, J. Ortyl, Photoinitiating systems and kinetics of frontal photopolymerization processes–the prospects for efficient preparation of composites and thick 3d structures, Polymer Chemistry 12 (32) (2021) 4593–4612.

[13] K. Kim, J. Sinha, G. Gao, K. K. Childress, S. M. Sartor, A. M. Salazar, S. Huang, C. B. Musgrave, J. W. Stansbury, High-efficiency radical photopolymerization enhanced by autonomous dark cure, Macromolecules 53 (13) (2020) 5034–5046.

[14] J. Wu, Z. Zhao, C. M. Hamel, X. Mu, X. Kuang, Z. Guo, H. J. Qi, Evolution of material properties during free radical photopolymerization, Journal of the Mechanics and Physics of Solids 112 (2018) 25–49.

[15] M. Lang, S. Hirner, F. Wiesbrock, P. Fuchs, A review on modeling cure kinetics and mechanisms of photopolymerization, Polymers 14 (10) (2022) 2074.

[16] T. Rehbein, M. Johlitz, A. Lion, K. Sekmen, A. Constantinescu, Temperature-and degree of cure-dependent viscoelastic properties of photopolymer resins used in digital light processing, Progress in Additive Manufacturing 6 (4) (2021) 743–756.

[17] J. Yue, X. Jiazhong, X. Kaixiang, L. Meijun, Mechanism characterization and multiphysics predictive modeling of photo-thermal coupled curing in gfrp, Polymer Testing (2026) 109095.

[18] T. Hafkamp, G. van Baars, B. de Jager, P. Etman, Real-time feedback controlled conversion in vat photopolymerization of ceramics: A proof of principle, Additive Manufacturing 30 (2019) 100775.

[19] M. Singh, J. Zhang, K. Bethel, Y. Liu, E. M. Davis, H. Zeng, Z. Kong, B. N. Johnson, Closed-loop controlled photopolymerization of hydrogels, ACS Applied Materials & Interfaces 13 (34) (2021) 40365–40378.

[20] L. Zhao, Z. Zhao, L. Ma, S. Li, Z. Men, L. Wu, Developing the optimized control scheme for digital light processing 3d printing by combining numerical simulation and machine learning-guided temperature prediction, Journal of Manufacturing Processes 132 (2024) 363–374.

[21] Y. Zhang, H. Zhang, X. Zhao, In-situ interferometric curing monitoring for digital light processing based vat photopolymerization additive manufacturing, Additive Manufacturing 81 (2024) 104001.

[22] I. Sachdeva, S. Ramesh, U. Chadha, H. Punugoti, S. K. Selvaraj, Computational ai models in vat photopolymerization: a review, current trends, open issues, and future opportunities, Neural Computing and Applications 34 (20) (2022) 17207–17229.

[23] Y. Kim, S. Sobhani, Nonlinear light attenuation curing effects in vat photopolymerization, Additive Manufacturing 109 (2025) 104857.

[24] P. Gkertzos, A. Kotzakolios, I. Katsidimas, S. Zaidi, D. Sanchez-Rodriguez, J. Costa, V. Kostopoulos, Comparative fitting methodology of cure kinetics models based on differential scanning calorimetry, Journal of Composite Materials 59 (1) (2025) 75–98.

[25] M. T. H. Nguyen, J. H. Kim, W. T. Jang, Y. J. Jung, E. J. Park, T. H. Ha, S. J. Ahn, Y. H. Kim, Role of go and photoinitiator concentration on curing behavior of peg-based polymer for dlp 3d printing, ACS omega 9 (3) (2024) 3287–3294.

[26] R. Setter, S. Schmölzer, N. Rudolph, E. Moukhina, K. Wudy, Thermal stability and curing behavior of acrylate photopolymers for additive manufacturing, Polymer Engineering & Science 63 (7) (2023) 2180–2192.